Inverse Problems 13 (1997) 1621–1639. Printed in the UK PII: S0266-5611(97)81805-9

Subsurface imaging with broadband electromagnetic induction

Alan Witten†, I J Won‡ and Stephen J Norton§

† School of Geology and Geophysics, The University of Oklahoma, 810 Energy Center, Norman, OK 73019-0628, USA

‡ Geophex Ltd, 605 Mercury St, Raleigh, NC 27603-2348, USA

§ Energy Division, Oak Ridge National Laboratory, PO Box 2008, Oak Ridge, TN 37831-6200, USA

Received 7 February 1997, in final form 11 August 1997

Abstract. Diffraction tomography (DT) is a quantitative technique for high-resolution subsurface imaging. In general, DT algorithms are used for subsurface imaging with propagating waves. In this study an imaging algorithm is developed and tested for use with broadband electromagnetic induction for a so-called 'multimonostatic' measurement geometry; a primary and secondary coil are coincident and move in unison over a uniformly spaced grid, on or above the ground surface. The algorithm is formulated in three dimensions and tested on simulated data for inhomogeneities that are both two and three dimensional. The algorithm is also applied, in two dimensions, to data acquired over a pair of parallel tunnels. One important finding is that good images can be reconstructed when the frequency band is limited to the case where all skin depths are greater than the depth of inhomogeneities.

1. Introduction

Since the early 1980s (Devaney 1982), work has been proceeding on the development of a class of high-resolution imaging algorithms that has become known as diffraction tomography (DT). The earliest concepts for geophysical diffraction tomography (GDT) (Devaney 1984) were for transmission-mode measurements—either offset vertical seismic profiling or cross-borehole—where tomographic images are reconstructed for a fixed frequency of illuminating wave.

In a parallel development, Won (1980) showed that broadband electromagnetic induction (EMI) could be used to perform vertical soundings of the Earth. By moving a coil pair along or above the ground surface and acquiring data over a broad range of frequencies at each coil location, a defocused image will result from displaying the secondary coil output as a function of skin depth and horizontal coil position. To illustrate this, consider an isolated conductive anomaly at some depth d in a homogeneous background and a coil pair fixed on the ground surface directly above the inhomogeneity. Increasing the skin depth δ (decreasing the driving frequency) from some small value to successively larger values, such that δ remains less than d, will not produce any significant change in the measured secondary field. This is because: (1) the background conductivity is constant; and (2) both the primary and secondary field decay exponentially with the skin depth so that the conducting anomaly is exposed to a very weak primary field that, in turn, produces a weak secondary field that undergoes substantial decay between the anomaly and the ground

0266-5611/97/061621+19$19.50

surface. The secondary field strength is some weighted average of the vertical variations in conductivity over the skin depth. Consequently, as δ is increased to the point where it is comparable to d, the inhomogeneity produces a perturbation in the secondary field. As δ increases beyond d, the vertical extent of the anomaly occupies a decreasing fraction of the skin depth and the secondary field becomes progressively weaker. Since the field from a dipole coil diminishes by geometric spreading at a rate inversely proportional to the distance cubed, moving the coil pair laterally away from the inhomogeneity and repeating the sounding yields an attenuated and, since the field propagates as well as decays with distance, perhaps, phase-shifted replicate of the sounding taken directly over the inhomogeneity. Thus, the display of broadband EMI data as a function of measurement position and skin depth essentially produces a blurred image of the anomaly that peaks at the lateral location of the anomaly and at a skin depth comparable to the target depth.

More recently, DT algorithms have been developed for ground penetrating radar (Molyneux and Witten 1993, Witten *et al* 1994). This work considers broadband electromagnetic wave illumination in a multimonostatic measurement geometry. Since the multimonostatic geometry assumed in the above cited radar-based imaging algorithms is the same as that typically employed in EMI data acquisition, it would seem that these radar algorithms could be extended to the case of a complex background wavenumber and thereby allow imaging with broadband EMI. However, there exists decades of experience in processing wave-based data; and consequently, optimal spatial and temporal sampling is well known. Specifically, in wave-based methods, it is necessary to sample spatially at intervals no greater than one-half of a wavelength. In geophysical EMI measurements, the wavelength is quite large so that the wave characteristics can be resolved with a coarse spatial sampling. It is expected that sampling based on the Nyquist criterion will not yield well resolved images and it remains to establish rules for optimal spatial sampling for EMI imaging. Because most EMI tools operate at relatively low frequencies, up to tens of kHz, an issue of particular importance is whether inhomogeneities; having characteristic depths less than the skin depth associated with the highest frequency, can be imaged.

In this study, a DT-based imaging algorithm is developed for broadband, multimonostatic imaging with EMI. A forward model (Witten *et al* 1994) is first presented that serves as the basis for the subsequent imaging algorithm. This algorithm is then applied to both synthetic and actual field data.

2. The forward model

The background geometry considered (figure 1) is a unform isotropic space characterized by constant dielectric ϵ_0, susceptibility μ_0, and conductivity σ_0, in which is embedded some localized imhomogeneity characterized by a spatially-variable conductivity, $\sigma(\boldsymbol{r})$ (and, perhaps $\epsilon(\boldsymbol{r})$) having support in the half-space $z < 0$. The governing equation for an electric field $\boldsymbol{E}$ driven at a frequency ω is derived from Maxwell's equations

$$(\nabla \times \nabla \times -k_0^2)\boldsymbol{E} = f(\boldsymbol{r})\boldsymbol{E} \tag{1}$$

where $k_0^2 = \mathrm{i}\omega\mu_0(-\mathrm{i}\omega\epsilon_0 + \sigma_0)$ is the background square wavenumber and inhomogeneities are characterized by the object function $f(\boldsymbol{r}) = \mathrm{i}\omega\mu_0(-\mathrm{i}\omega[\epsilon(\boldsymbol{r}) - \epsilon_0] + [\sigma(\boldsymbol{r}) - \sigma_0])$. For simplicity, a low-frequency approximation is assumed where $\sigma(\boldsymbol{r}), \sigma_0 \gg \omega\epsilon(\boldsymbol{r}), \omega\epsilon_0$, so that

$$k_0 \approx \sqrt{\mathrm{i}\omega\mu_0\sigma_0} \tag{2}$$

and

$$f(\boldsymbol{r}) \approx \mathrm{i}\omega\mu_0[\sigma(\boldsymbol{r}) - \sigma_0] = k_0^2\left[\frac{\sigma(\boldsymbol{r})}{\sigma_0} - 1\right] = k_0^2 O(\boldsymbol{r}) \tag{3}$$

where $O(\boldsymbol{r})$ is referred to as the object function.

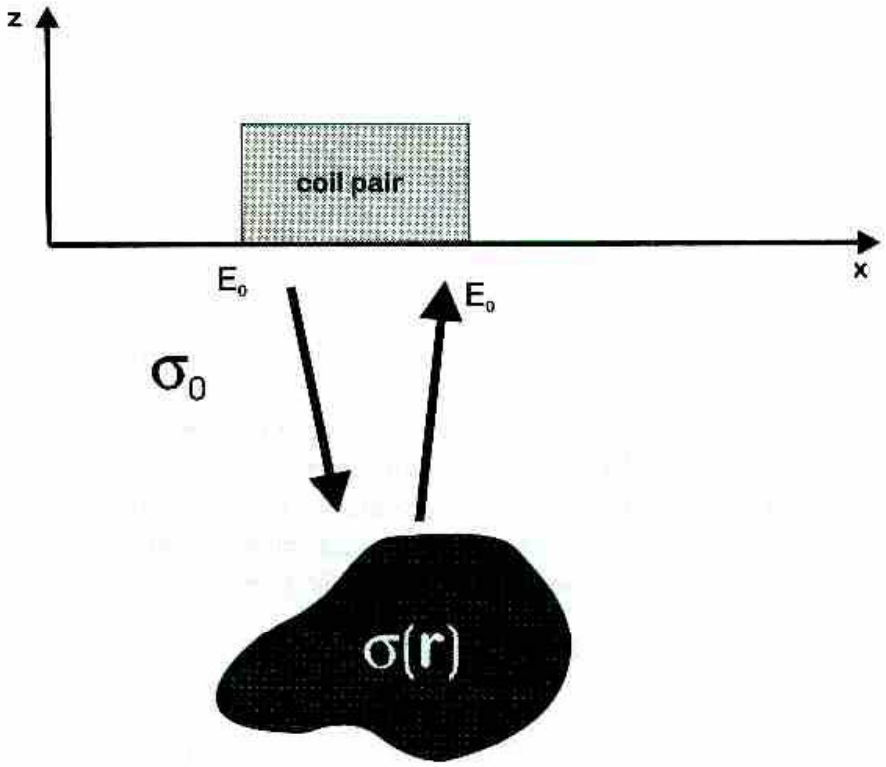

Figure 1. The host geometry under consideration. The y axis (not shown) is into the plane of the figure. A co-located transmitting and receiving coil is located in the box labelled coil pair. Each coil is assumed to have an arbitrary orientation.

Equation (1) can be expressed in the form of an integral equation for the secondary field $\boldsymbol{E}_s$ as

$$\boldsymbol{E}_s(\boldsymbol{r}) = \int \mathrm{d}\boldsymbol{r}'\, \boldsymbol{E}(\boldsymbol{r}') \cdot \mathcal{G}(\boldsymbol{r} - \boldsymbol{r}') f(\boldsymbol{r}') \tag{4}$$

where $\mathcal{G}$ is the dyadic Green function. Assuming that $z' < z$, which will be the case when measurements are made on or above the ground surface and the support of f is entirely in the lower half-space (figure 1), $\mathcal{G}$ can be expressed as the Weyl-type expansion (Morse and Feshbach 1953)

$$\mathcal{G}(\boldsymbol{r} - \boldsymbol{r}') = \frac{\mathrm{i}}{8\pi^2} \int \mathrm{d}\boldsymbol{K}\, \frac{1}{m} (\mathcal{I} - \hat{\boldsymbol{k}}_+ \hat{\boldsymbol{k}}_+)\, \mathrm{e}^{\mathrm{i}\boldsymbol{k}_+ \cdot (\boldsymbol{r} - \boldsymbol{r}')} \tag{5}$$

where $\mathcal{I}$ is the identity dyad, $\boldsymbol{k}_+ = \boldsymbol{K} + m(\boldsymbol{K})\hat{\boldsymbol{z}}$, $m(\boldsymbol{K}) = \sqrt{k_0^2 - |\boldsymbol{K}|^2}$, the imaginary part of $m \geqslant 0$, the hatted quantities are unit vectors, and $\boldsymbol{K}$ is the two-dimensional horizontal wavevector.

By assuming that the electric field $\boldsymbol{E}$ changes slowly over the support volume of $f(\boldsymbol{r})$, the volume over which $f(\boldsymbol{r}) \neq 0$, the field appearing under the integral in (4) can be replaced by the primary field $\boldsymbol{E}_0$. This is the Born approximation. The primary field at some $\boldsymbol{r}'$ with $z' < 0$ can be represented in terms of the primary field at $z = 0$ by

$$\boldsymbol{E}_0(\boldsymbol{r}') = \frac{1}{(2\pi)^2} \int \mathrm{d}\boldsymbol{K}' \, \mathrm{e}^{\mathrm{i}\boldsymbol{k}'_- \cdot \boldsymbol{r}'} \tilde{\boldsymbol{E}}_0(\boldsymbol{K}', z = 0) \tag{6}$$

where $\tilde{\boldsymbol{E}}_0$ is the two-dimensional, horizontal Fourier transform of $\boldsymbol{E}_0$

$$\tilde{\boldsymbol{E}}_0(\boldsymbol{K}', z) = \int \mathrm{d}\boldsymbol{x}' \, \mathrm{e}^{-\mathrm{i}\boldsymbol{K}' \cdot \boldsymbol{x}'} \boldsymbol{E}_0(\boldsymbol{x}', z) \tag{7}$$

$\boldsymbol{r}' = (\boldsymbol{x}', z')$ and $\boldsymbol{k}'_- = \boldsymbol{K}' - m(\boldsymbol{K}')\hat{\boldsymbol{z}}$.

Invoking the Born approximation, taking the primary coil to be located at point $\boldsymbol{r}_0$ and using (5) and (6) in (4); the horizontally Fourier-transformed secondary field becomes

$$\begin{aligned} \tilde{\boldsymbol{E}}_s(\boldsymbol{K}, z; \boldsymbol{r}_0) &= \int \mathrm{d}\boldsymbol{x} \, \boldsymbol{E}_s(\boldsymbol{x}, z) \, \mathrm{e}^{-\mathrm{i}\boldsymbol{K} \cdot \boldsymbol{x}} \\ &= \mathrm{e}^{\mathrm{i}mz} (\mathcal{I} - \hat{\boldsymbol{k}}_+ \hat{\boldsymbol{k}}_+) \cdot \frac{\mathrm{i}}{2m} \int \mathrm{d}\boldsymbol{K}' \, \tilde{\boldsymbol{E}}_0(\boldsymbol{K}', 0) \, \mathrm{e}^{-\mathrm{i}\boldsymbol{k}'_- \cdot \boldsymbol{r}_0} \int \mathrm{d}\boldsymbol{r}' \, f(\boldsymbol{r}') \, \mathrm{e}^{-\mathrm{i}(\boldsymbol{k}_+ - \boldsymbol{k}_-) \cdot \boldsymbol{r}'} \end{aligned} \tag{8}$$

and $\tilde{\boldsymbol{E}}_0(\boldsymbol{K}', 0)$ characterizes the coil used to generate the primary field.

The next steps in the development of the forward model formulation involve the representation of the transmitter and receiver coils in terms of their orientations and their input and output characteristics. The open terminal output voltage from the receiver coil resulting from its response to a secondary field $\boldsymbol{E}_s$ is given by

$$V_{oc}(\boldsymbol{r}_0) = -\frac{1}{I_0} \int \mathrm{d}\boldsymbol{r}' \, \boldsymbol{J}(\boldsymbol{r}') \cdot \boldsymbol{E}_s(\boldsymbol{r}' + \boldsymbol{r}_0) \tag{9}$$

where I_0 is the current across the coil terminals and $\boldsymbol{J}(\boldsymbol{r}')$ is the current distribution within the coil. It has been assumed that the receiver coil is coincident with the transmitter coil at $\boldsymbol{r}_0$.

The vector magnetic potential for a current distribution $\boldsymbol{J}_0$ in the transmitter coil is given by

$$\boldsymbol{A}(\boldsymbol{r}) = \mu_0 \int \mathrm{d}\boldsymbol{r}' \, \boldsymbol{J}_0(\boldsymbol{r}') G(\boldsymbol{r} - \boldsymbol{r}') \tag{10}$$

where

$$G(\boldsymbol{r} - \boldsymbol{r}') = \frac{\mathrm{i}}{8\pi^2} \int \mathrm{d}\boldsymbol{K}' \, \frac{1}{m(\boldsymbol{K}')} \, \mathrm{e}^{\mathrm{i}\boldsymbol{k}'_- \cdot (\boldsymbol{r} - \boldsymbol{r}')}. \tag{11}$$

Using the relationship between the magnetic potential and electric field

$$\boldsymbol{E} = \frac{\mathrm{i}}{\omega \mu_0 \epsilon_0} \nabla \times \nabla \times \boldsymbol{A} \tag{12}$$

the two-dimensional, horizontally Fourier-transformed primary field can be written as

$$\tilde{\boldsymbol{E}}_0(\boldsymbol{K}, z) = -\frac{\omega \mu_0}{2m} (\mathcal{I} - \hat{\boldsymbol{k}}_- \hat{\boldsymbol{k}}_-) \cdot \int \mathrm{d}\boldsymbol{r}' \, \boldsymbol{J}_0(\boldsymbol{r}') \, \mathrm{e}^{-\mathrm{i}\boldsymbol{k}_- \cdot \boldsymbol{r}'}. \tag{13}$$

The final introduction of coil-specific parameters is made by assuming that a coil (either the transmitter or receiver) is of small radius a, consisting of N turns with its axis pointing in the direction $\hat{\boldsymbol{n}}$, and is located at some elevation above the ground surface $h \geqslant 0$. By taking the current to be constant within the coil,

$$(\mathcal{I} - \hat{\boldsymbol{k}}_\pm \hat{\boldsymbol{k}}_\pm) \cdot \int \mathrm{d}\boldsymbol{r}' \, \boldsymbol{J}(\boldsymbol{r}') \, \mathrm{e}^{\pm \mathrm{i}\boldsymbol{k}_\pm \cdot \boldsymbol{r}'} = \pm \mathrm{i}\pi N a^2 \, \mathrm{e}^{\mathrm{i}mh} \hat{\boldsymbol{n}} \times \hat{\boldsymbol{k}}_\pm. \tag{14}$$

Substituting (9), (13) and (14) into (8) yields the final form of the forward model

$$\tilde{V}_{oc}(\boldsymbol{K}) = -i\omega\mu_0(\pi k_0)^4 \int d\boldsymbol{K}' \, (e^{iQh}/Q) H(\boldsymbol{K}, \boldsymbol{K}'; \boldsymbol{k}_+) \int d\boldsymbol{r}' \, O(\boldsymbol{r}') \, e^{-i(\boldsymbol{K}\cdot\boldsymbol{x}+Qz)} \tag{15}$$

where $\tilde{V}_{oc}(\boldsymbol{K})$ is the horizontally Fourier-transformed output voltage,

$$Q = m(\boldsymbol{K}/2 + \boldsymbol{K}') + m(\boldsymbol{K}/2 - \boldsymbol{K}')$$

N_s is the number of turns in the receiver coil, N_0 is the number of turns in the transmitter coil, a_s is the radius of the receiver coil, a_0 is the radius of the transmitter coil,

$$H(\boldsymbol{K}, \boldsymbol{K}'; \boldsymbol{k}_+) = I_0 N_s N_0 a_s^2 a_0^2 [\hat{n}_s \times \hat{k}_+(\boldsymbol{K}' + \boldsymbol{K}/2)] \cdot [\hat{n}_0 \times \hat{k}_+(\boldsymbol{K}' - \boldsymbol{K}/2)] \tag{16}$$

and $\hat{n}_s$ and $\hat{n}_0$ are the unit vectors defining the direction of the axis of the receiver and transmitter coils, respectively. Equation (15) assumes that the coils are imbedded in a material having the same conductivity as the material that hosts the support of $O(\boldsymbol{r})$. A two-layer system, such as air over soil or rock, is considered in appendix A.

3. Inversion and imaging

The inner integral in (15) is a spatial Fourier transform of the object function O. This form of the forward model is similar to a 'generalized projection slice theorem' (GPST) of diffraction tomography. GPSTs are analytic relationships between the spatial Fourier transform of the acquired data and the spatial Fourier transform of the object function. With a GPST, imaging can be accomplished by inversion using standard numerical techniques. The forward model defined by (15) is not suitable for such an inversion due to the outer ($\boldsymbol{K}'$) integration. Thus, it is necessary to seek some closed-form evaluation of this integral in order to derive a GPST for broadband EMI imaging.

The procedure employed here parallels that established by Molyneux and Witten (1993) whereby the outer integration in (15) is performed approximately by the stationary phase. This approximate representation is valid provided that $H/m(\boldsymbol{K}/2 + \boldsymbol{K}')m(\boldsymbol{K}/2 - \boldsymbol{K}')$ varies slowly compared to $[m(\boldsymbol{K}/2 + \boldsymbol{K}') + m(\boldsymbol{K}/2 - \boldsymbol{K}')](h - z)$ over some range of $\boldsymbol{K}$. This, in turn, requires that there be a large coefficient in the exponential of the integrand and this will be the case when $(h - z)$ is much greater than one-half of the skin depth δ where $\delta = 1/\sqrt{\sigma_0\mu_0\omega}$. Rigorously, at least in the forward sense, this weak far-field approximation may limit the applicability of this imaging algorithm; however, Molyneux and Witten (1993) demonstrated that no such limitation exists in the inverse sense. It is hoped that this finding can be generalized to the case of EMI inversion considered here. Performing the $\boldsymbol{K}'$ integration in (15) by stationary phase yields the approximate relationship

$$\tilde{V}_{oc}(\boldsymbol{K}) \approx \tfrac{1}{2}\omega\mu_0 k_0^2 \pi^5 \bar{H}(\boldsymbol{k}) \gamma(\boldsymbol{K}) \, e^{i\gamma h} \bar{\tilde{O}}_1(\boldsymbol{k}) \tag{17}$$

where

$$\gamma(\boldsymbol{K}) = \sqrt{4k_0^2 - |\boldsymbol{K}|^2}$$

$$\boldsymbol{k} = \boldsymbol{K} + \gamma(\boldsymbol{K})\hat{z}$$

$$\bar{\tilde{O}}_1(\boldsymbol{k}) = \int d\boldsymbol{r} \, \frac{O(\boldsymbol{r})}{(h - z)} e^{-i\boldsymbol{k}\cdot\boldsymbol{r}} = \int dz \, \frac{e^{-i\gamma z}}{h - z} \int d\boldsymbol{x} \, O(\boldsymbol{x}, z) \, e^{-i\boldsymbol{K}\cdot\boldsymbol{x}} = \int dz \, \frac{e^{-i\gamma z}}{h - z} \tilde{O}(\boldsymbol{K}, z)$$

$$\tilde{O}(\boldsymbol{K}, z) = \int d\boldsymbol{x} \, O(\boldsymbol{x}, z) \, e^{-i\boldsymbol{K}\cdot\boldsymbol{x}} \tag{18}$$

and

$$\bar{H}(\boldsymbol{k}) = I_0 N_0 N_s a_0^2 a_s^2 (\hat{\boldsymbol{n}}_0 \times \boldsymbol{k}) \cdot (\hat{\boldsymbol{n}}_s \times \boldsymbol{k}) \tag{19}$$

is a coil-specific filter function.

Equation (17) is the final form of the GPST for broadband EMI imaging. This equation can be rewritten as

$$\bar{\bar{O}}_1(\boldsymbol{k}) = \frac{2}{\omega \mu_0 \pi^5 k_0^2 \gamma(\boldsymbol{K}) \bar{H}(\boldsymbol{k})} e^{-i\gamma h} \tilde{V}_{oc}(\boldsymbol{K}) \tag{20}$$

to explicitly represent O_1 as a function of V_{oc}. An image of the spatial variations in O_1 and, hence, O or $\sigma(\boldsymbol{r})$ can be reconstructed by inverting the integral transform

$$\bar{\bar{O}}_1(\boldsymbol{k}) = \int d\boldsymbol{x}\, e^{-i\boldsymbol{K}\cdot\boldsymbol{x}} \tilde{O}_1(\boldsymbol{x}, \boldsymbol{k}) \tag{21}$$

where

$$\tilde{O}_1(\boldsymbol{x}, \boldsymbol{k}) = \int dz\, O_1(\boldsymbol{x}, z) e^{-i\gamma z}. \tag{22}$$

Equation (21) is a horizontal, two-dimensional, spatial Fourier transform that can be inverted by fast Fourier transform (FFT) techniques; however, (22) is a one-dimensional Fourier transform with a complex wavenumber γ and, therefore, cannot be inverted using an FFT. For this reason, the inversion is a two-step process where, in the first step, the integral transform

$$\bar{\bar{O}}_1(\boldsymbol{k}) = \int dz\, \tilde{O}_1(\boldsymbol{K}, z) \frac{e^{-i\gamma z}}{h - z} \tag{23}$$

is inverted and then $\tilde{O}_1(\boldsymbol{K}, z)$ is inverted by a standard two-dimensional FFT. Equation (23) is inverted by approximating the integral by the quadrature formula

$$\bar{\bar{O}}_1(\boldsymbol{K}, \gamma_i) \approx \sum_j A_{ij} \tilde{O}_1(\boldsymbol{K}, z_j) \tag{24}$$

where

$$A_{ij} = e^{-i\gamma_j z_i} \tag{25}$$

$$\gamma_i = \sqrt{4i\delta_i^{-2} - |\boldsymbol{K}|^2} \tag{26}$$

$$z_j = z_0 + (j-1)\Delta z$$

and

$$\delta_i = \delta_0 + (i-1)\Delta\delta.$$

Equation (24) represents a mapping from uniformly spaced sampling in z, beginning at a minimum depth z_0, in increments of Δz, into a uniformly spaced sampling in skin depth from δ_0, in increments of $\Delta\delta$.

Equation (24) could be solved by inverting the matrix A_{ij}; however, the system of equations is ill-conditioned so that it becomes necessary to seek a less direct method of inversion. The method used here is regularization where, rather than considering (24), the equation

$$\bar{\bar{O}}_1(\boldsymbol{K}, \gamma_i) = \sum_j (A_{ij} - \lambda I_{ij}) \tilde{O}_1(\boldsymbol{K}, z_j) \tag{27}$$

is inverted, where I_{ij} is the identity matrix and λ is referred to as the regularization parameter. The inversion of (27) must be optimized with respect to the regularization parameter. If λ is too small, the inversion will be unstable and if λ is too large, the image will be excessively blurred.

Following the inversion of (27) by regularization for each value of $\boldsymbol{K}$, $O_1(\boldsymbol{r})$ can be computed by inversion of the two-dimensional Fourier transform. The object function can be reconstructed from $O(\boldsymbol{r}) = (h - z)O_1$ and the spatial variations in conductivity can, in turn, be computed using $\sigma(\boldsymbol{r}) = \sigma_0(O(\boldsymbol{r}) + 1)$.

4. Results

The forward model derived in section 2 and the inversion algorithm derived in section 3 are three dimensional and allow arbitrary primary and secondary coil orientations. These developments are restricted to cases where both coils are in intimate contact with the ground surface. For situations where the coils are above the ground surface, the formulation is slightly more complicated and the forward model for this case is given in appendix A. This model can be used to develop an inversion algorithm following the procedure given in section 3. For all the results presented in this section, a standard numerical scheme (Press *et al* 1992) was used to implement the regularized inversion defined in (27).

4.1. Two-dimensional synthetic data

Images from broadband EMI are presented using (17) to simulate the broadband data, and (20) and (27) are used to reconstruct the image. For simplicity, the targets are taken to be two dimensional, varying only in the x, z plane, and only three coil orientations are considered. These are: vertical coils—both coil axes are vertical, $\hat{\boldsymbol{n}}_0 = \hat{\boldsymbol{n}}_s = (0, 0, 1)$; horizontal coils—both coil axes are horizontal and parallel to the transect line, $\hat{\boldsymbol{n}}_0 = \hat{\boldsymbol{n}}_s = (1, 0, 0)$; and horizontal coplanar coils—both coil axes are horizontal and perpendicular to the transect line, $\hat{\boldsymbol{n}}_0 = \hat{\boldsymbol{n}}_s = (0, 1, 0)$.

Extensive testing was performed on all coil orientations for a variety of targets of simple shapes. Since the vertical coil orientation produces a smaller gradient in the vertical field and a larger gradient in the horizontal field, as compared to either of the horizontal coil orientations, the forward model results exhibited noticeable differences with varying coil orientation. In contrast, reconstructed images were quantitatively similar for all coil orientations and target shapes. For this reason, the results presented here are limited to those associated with variations in the parameters that affect the quality of reconstructed images: these are the choice of regularization parameter λ (27) and the skin depth interval. For all results presented, a horizontal coil orientation was assumed, the inhomogeneity was a 16 by 4 rectangular conducting anomaly centred at $(0, -16)$, and data were synthesized at 32 horizontal measurement points at $z = 0$ and uniformly distributed over the interval $[-32, 30]$.

Figure 2 provides simulated results for the above described target and measurement configuration displaying the effects of varying the regularization parameter. It is expected that, for relatively large values of this parameter, the inversion should be quite stable; however, the image will be blurred as a result of excessive smoothing. For an extremely small regularization parameter, the inversion will be unstable. Figure 2(a) is the real part of the simulated data where the vertical axis is skin depth. For the simulations presented in this figure, 16 skin depths uniformly distributed on the interval $[2, 32]$ were used. As established by Won (1980), the simulated data appear as an out-of-focus image of the

rectangular target, with the target appearing as a negative anomaly. The reconstructed images, figures 2(b) through 2(e), exhibit the expected result of increased image sharpness with decreasing regularization parameter. An important finding is that the inversion is quite stable and reasonable images were reconstructed over a range of regularization parameter that spans six orders of magnitude.

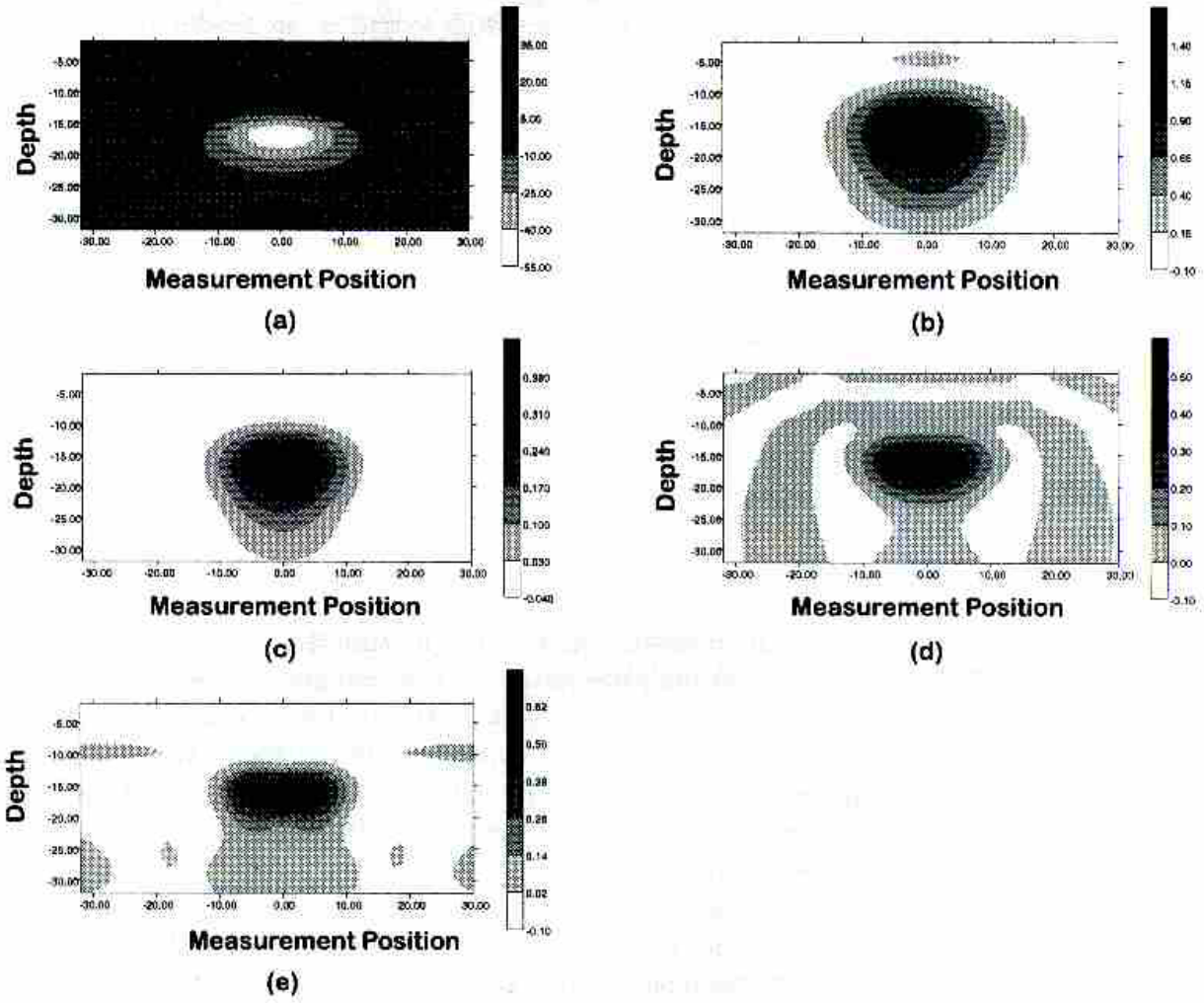

Figure 2. Data and images of a 16 × 4 conducting rectangle centred at $(0, -16)$ for 32 measurement points uniformly distributed over the interval $[-32, 30]$ along the ground surface, 16 skin depths uniformly distributed on $[2, 32]$ and a horizontal coil axis for (a) the real part of the simulated data and images for regularization parameters of (b) $1e-4$, (c) $1e-6$, (d) $1e-8$, and (e) $1e-10$.

Figures 3 and 4 are reconstructed images displaying the effect of varying the skin depth interval. For all reconstructions, data based on 16 skin depths were used. Figure 3 demonstrates the effect of broadening the range of skin depths and, in this figure, the minimum skin depth is always significantly less than the depth of the conducting rectangle, while the maximum skin depth is progressively increased from 8 (figure 3(a)) to 128 (figure 3(e)). Poor images are obtained when the maximum skin depth is less than the deepest extent of the inhomogeneity (figures 3(a) and (b)). For a maximum skin depth of 8 (figure 3(a)), the reconstructed rectangle has the proper shape, but is too shallow, and increasing the maximum skin depth to 16 (figure 3(b)) results in a reconstruction of the rectangle that is somewhat deeper; however, it is still too shallow and the contrast is reversed. Increasing the maximum skin depth to 24 (figure 3(c)) results in a reasonable reconstruction.

The reconstructed image is excellent for a maximum skin depth of 48 (figure 3(d)) and even at a maximum skin depth of 128 (figure 3(d)) the reconstructed image is quite good. This is a somewhat surprising result, since for 16 skin depths uniformly distributed on the interval [2, 128], the skin depth increment is almost 8, which is twice the thickness of the rectangular anomaly. While skin depth is somewhat analogous to time in wave-based methods, it is clear that a reflector may be entirely absent in the data for a coarse time sampling; however, such a coarse sampling in skin depths does not profoundly impact the quality of the EMI images.

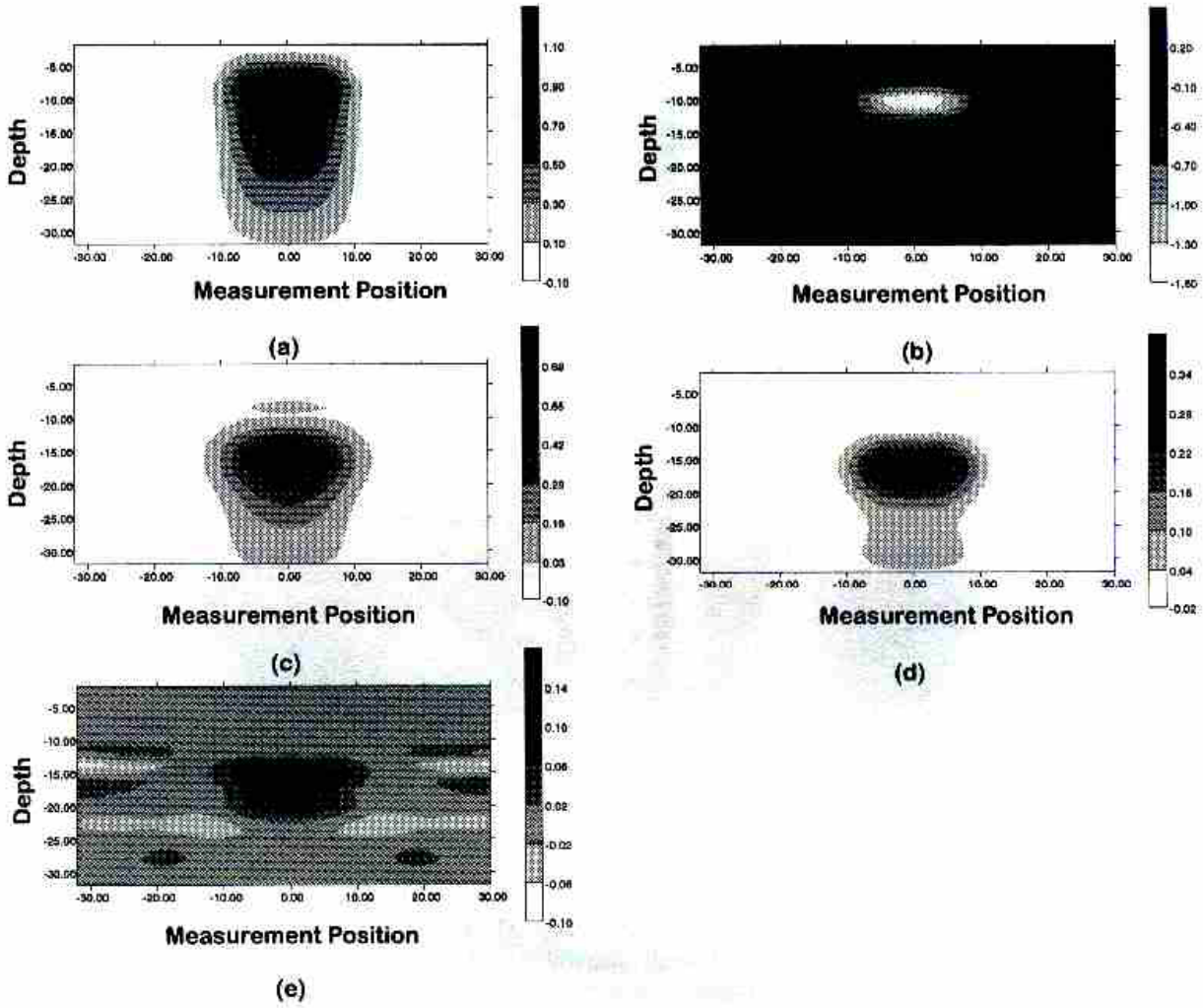

Figure 3. Images of a 16×4 conducting rectangle centred at $(0, -16)$ for 32 measurement points uniformly distributed on the interval $[-32, 30]$ along the ground surface, a regularization parameter of $1e-8$, a horizontal coil axis, and 16 skin depths uniformly distributed over (a) $[1, 8]$, (b) $[1, 16]$, (c) $[2, 24]$, (d) $[2, 48]$, and (e) $[2, 128]$.

Figure 4 demonstrates the effects of simultaneously varying the minimum skin depth and the skin depth interval. The purpose of these simulations is to investigate implications of using a minimum skin depth that is greater than the target depth. Figure 4(a) is a reconstructed image for a minimum skin depth of 8 and a maximum skin depth of 32. Here, the range of skin depths spans the depth interval of the conductor and the reconstructed image is quite good. When the skin depth does not completely span the vertical extent of the target (figure 4(b)), the image is still good. This is in complete contrast to figure 3(b) where the deeper skin depths, rather than the shallower skin depths, are absent. Increasing the minimum skin depth (figure 4(c)) and further increasing the minimum skin depth and

broadening the skin depth interval (figure 4(d)) results in a progressive blurring of the image. The reason that skin depths less than the target depth are not required to adequately image inhomogeneities is apparent in the simulated data (figure 2(a)). It is clear in this figure that the gradient with respect to skin depth is much steeper for skin depths less than target depth, than for skin depths greater than the target depth. Furthermore, for skin depths less than about one-half the target depth, the secondary field is almost zero. For skin depths substantially larger than the target depth, the secondary field decays slowly with increasing skin depth and there is information regarding target structure encoded in these large skin depths.

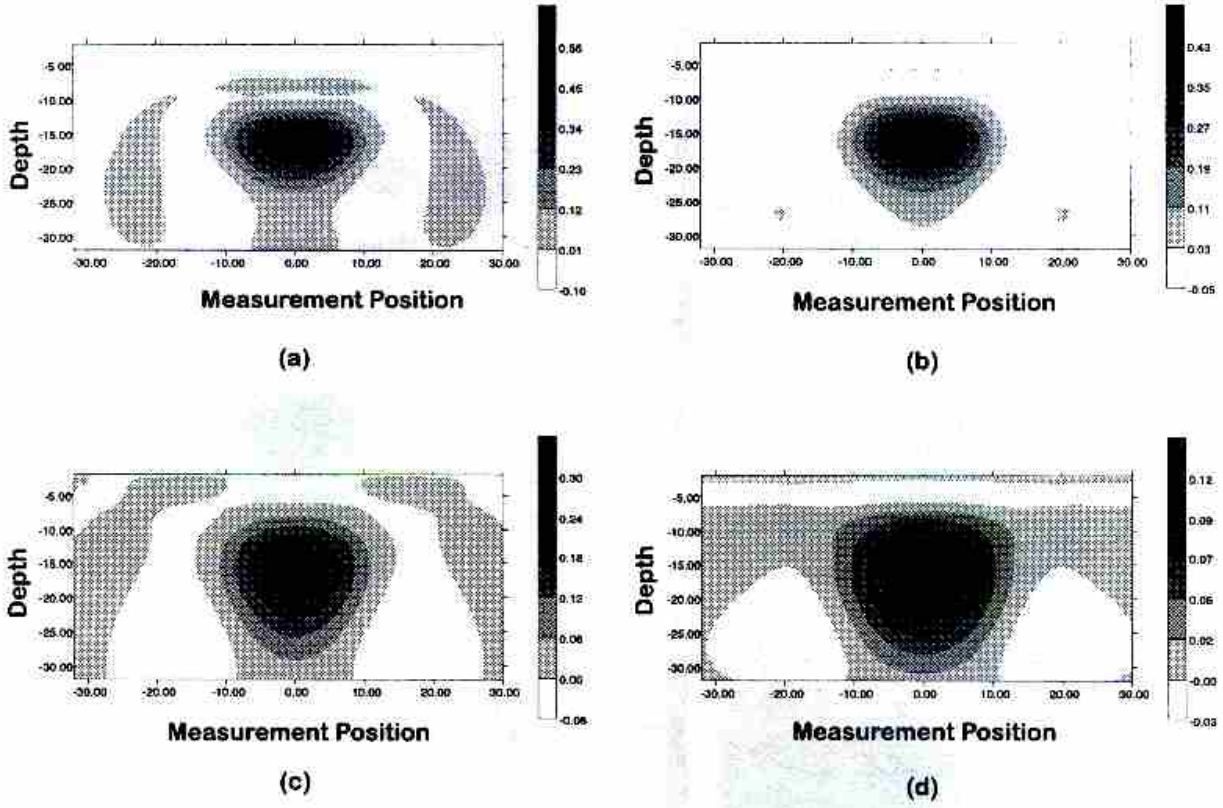

Figure 4. Images of a 16×4 conducting rectangle centred at $(0, -16)$ for 32 measurement points uniformly distributed on the interval $[-32, 30]$ along the ground surface, a horizontal coil axis, and 16 skin depths uniformly distributed over (a) $[8, 32]$, (b) $[16, 48]$, (c) $[32, 64]$, and (d) $[64, 128]$. The regularization parameter used for (a) and (b) is $1e-8$ and for (c) and (d) is $1e-6$.

While the images given above represent quite good reconstructions, they were obtained from noise-free simulated data. Since the inversion of (24) can be ill-conditioned, it can be expected that signal noise can have a profound impact on image quality, particularly when all skin depths are greater than the target depth. To address this problem, additional imaging was performed with noise added to the synthetic data. Two noise models were considered; the relative noise case where the signal-to-noise ratio was defined relative to the maximum signal at each skin depth, and the absolute noise case where the signal-to-noise ratio was defined relative to the maximum signal over all skin depths independent of the skin depths used in the image reconstruction. Noise was added to the signal by first generating a sequence of random numbers uniformly distributed over the interval $[-1, 1]$. After dividing by the signal-to-noise ratio, these random numbers were added to the simulated data. For both noise models, images were reconstructed for a variety of ranges of skin depths. The

results of these simulations are summarized below.

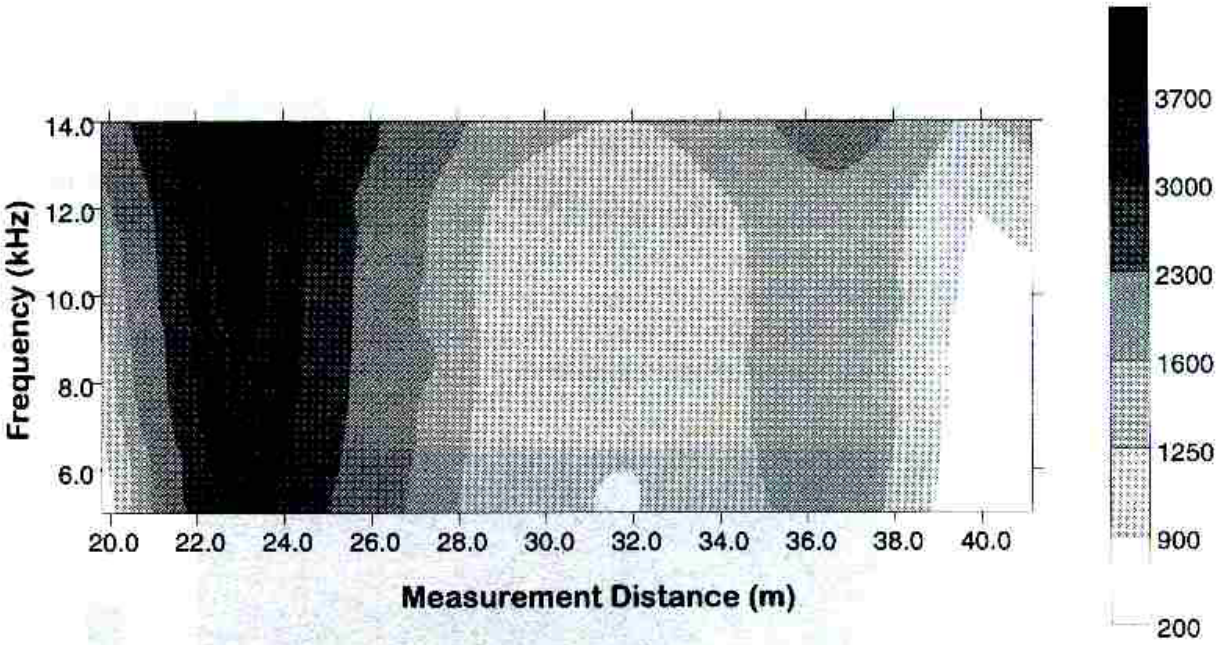

Figure 5. Plot of the real part of the ratio of primary to secondary field as a function of measurement location and frequency for EMI data acquired over the top of a pair of subway tunnels.

(1) Decreasing the signal-to-noise ratio produces a degradation in image quality that, to a point, can be offset by increasing the regularization parameter but with an associated loss of image sharpness.

(2) There is a signal-to-noise ratio lower limit below which the target cannot be reconstructed no matter how large the regularization parameter. These limiting signal-to-noise ratio values are about 100 and 20 for the absolute and relative noise models, respectively.

(3) Signal noise did not affect the images reconstructed for cases where all skin depths are greater than the target depth more than for cases where the skins depths span the target depth.

4.2. Two-dimensional field data

While the results based on synthetic data establish that images can be reconstructed when all skin depths are significantly greater than the target depth, it must be recognized that, as skin depths increase beyond the target depth, the magnitude of the secondary field decreases substantially. Since the signal-to-noise ratio for synthetic data is essentially infinite, an important issue related to the viability of geophysical EMI imaging is whether adequate images can be reconstructed for large skin depths when the signal-to-noise ratio is finite, or more importantly, small. The synthetic data examples considered here use the forward model given by (17) and, as such, do not address the issue of the weak far-field approximation required to achieve the GPST. The validity of this approximation will be tested provided that all, or some, of the frequencies acquired correspond to skin depths greater than the depth of inhomogeneities.

To address these concerns, broadband EMI data were acquired along a line on the ground surface over a parallel pair of subway tunnels near the Washington, DC, Anacostia Metro station. The broadband geophysical tool used was the GEM-2 (Won *et al* 1996). A subset of this data set was used for imaging. Sixteen measurement points were uniformly distributed over the interval [18 m, 41 m] on the ground surface perpendicular to the axes of the tunnel pair. Sixteen frequencies uniformly distributed over the interval [5010 Hz, 14 010 Hz] were used in the reconstruction. Figure 5 is a display of the real part of the data as a function of measurement location and frequency. Since the range of frequencies shown is quite low, all skin depths are large. As a consequence, the data as displayed do not appear as an out-of-focus image, but rather only the tail of the gradient with respect to skin depth is evident. Thus, this data set represents a good test of both the impact of a low signal-to-noise ratio and the far-field approximation.

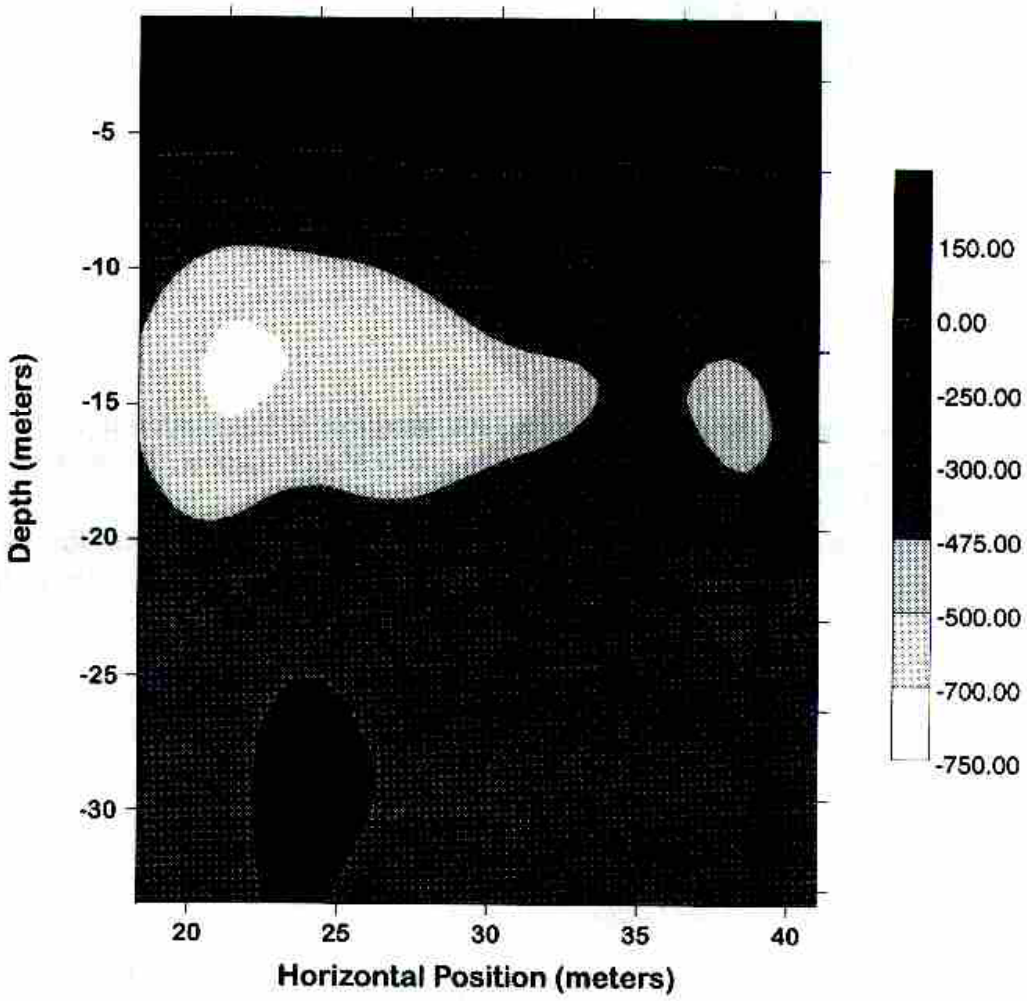

Figure 6. Reconstructed image of a pair of parallel subway tunnels near the Washington, DC, Anacostia Metro Station. The tunnel cross sections appear as the near-circular, low conductivity anomalies at a depth of about 12 m. The near-surface high conductivity layer is believed to be saturated soil.

Figure 6 is the image reconstructed from these data based on a regularization parameter of $1e-6$ and an assumed background conductivity of 0.1 Siemen m^{-1}. The cross sections of the two tunnels are clearly evident as the near-circular low conductivity anomalies at a depth of about 12 m. In addition, there is an apparent high conductivity layer in the upper 3 m of the image. There was standing water on the ground at the time the data were

acquired, getting progressively deeper to about 0.3 m at one end of the measurement line (the right-hand side of figure 5), and this layer is likely a result of the presence of surface and near-surface water. The depth of the tunnels at the measurement line is not known, however, their imaged depth is consistent with available estimates.

4.3. Three-dimensional synthetic data

To demonstrate EMI imaging in three dimensions, broadband EMI data was synthesized for measurements made over a two-dimensional grid on the ground surface. A 16×16 grid was employed, where $-16 \leqslant x, y \leqslant 14$. The target was a rectangular solid conductor with centre at $(0, 0, -16)$ and having dimensions $(8, 16, 4)$. Data were synthesized for eight skin depths uniformly distributed on the interval $[2, 32]$. The three-dimensional reconstruction was based on eight depth points uniformly distributed on the interval $[-9, -23]$ and a regularization parameter of $1e-8$. Figure 7 is a 'chair cut' of the three-dimensional image through the centre of the inhomogeneity. This figure is an accurate representation of the target location and aspect ratio. While this image is not as sharp as the synthetic reconstructions for the two-dimensional rectangle, it must be recognized that this image is based on the equivalent of one-quarter of the data points used in the two-dimensional simulations.

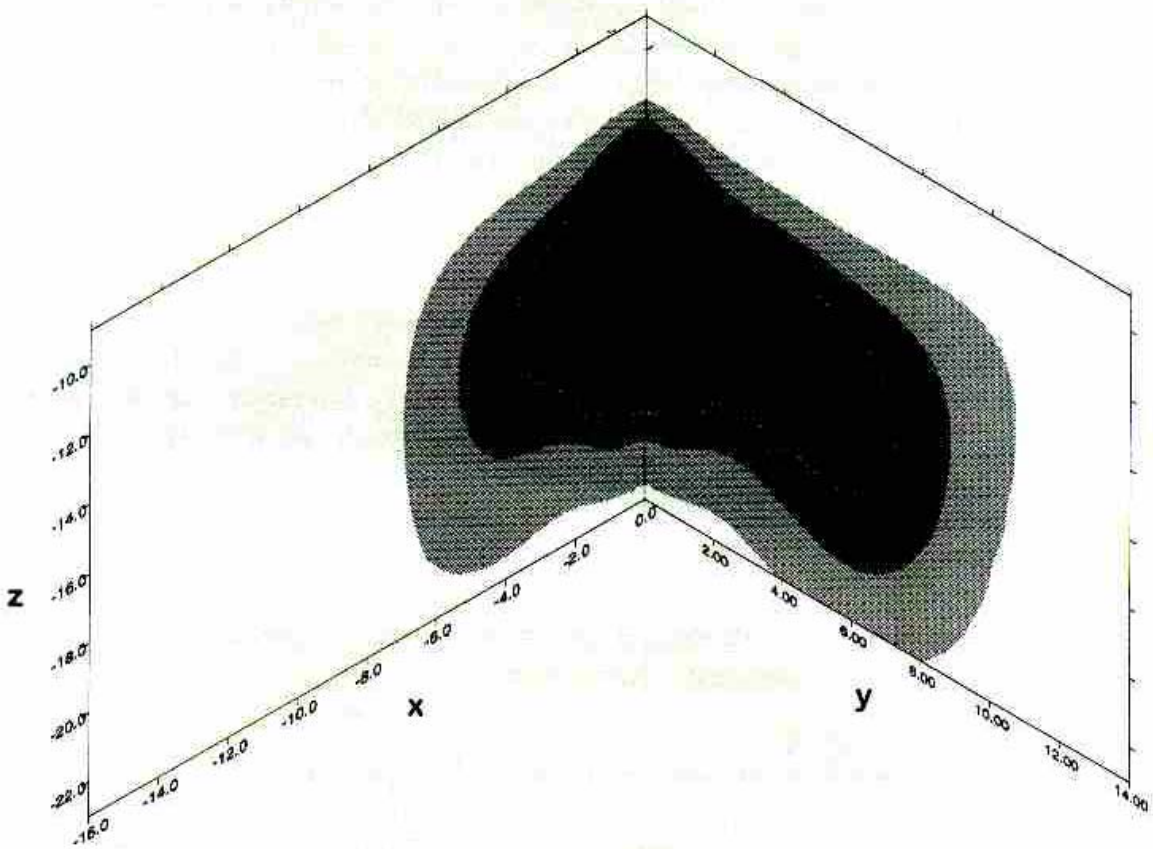

Figure 7. 'Chair cut' through a three-dimensional image of a reconstructed rectangular solid conductor.

5. Conclusions

A three-dimensional imaging algorithm for broadband EMI data has been developed and implemented. This algorithm has been tested on two- and three-dimensional synthetic data and on two-dimensional field data. It has been shown that EMI imaging can yield good reconstructions of both conductive and resistive targets, even for a relatively small number of frequencies. Perhaps the most important finding is that adequate images can be obtained when the highest frequency is so low that all skin depths are greater than the target depth. This is exemplified by the reconstructed image of the tunnels (figure 6) where the tunnels are manifested in the data as only a gradient in frequency (figure 5), rather than a well defined peak in response at a skin depth comparable to the target depth (figure 2(a)). This suggests that there is some hope for imaging relatively small and shallow targets with the relatively low-frequency EMI tools.

The imaging approach is based on the concept of diffraction tomography where an analytic relationship is established between the spatial Fourier transform of the acquired data and a spatial intregral transform of the variations in conductivity. For EMI imaging, the integral transform is Fourier (real wavenumber) in the horizontal directions while the vertical component of the integral transform is characterized by a complex wavenumber. For this reason, the full integral transform cannot be inverted by the computationally efficient fast Fourier transform procedure. The mapping from depth into skin depth must be inverted by matrix inversion at every horizontal wavevector point, which is far less efficient. Despite this limitation, the imaging algorithm is computationally efficient. For example, the three-dimensional image reconstruction required only several seconds on a Pentium-based processor. For production-mode processing where image depths and skin depths are fixed, the algorithm can be rendered more computationally efficient by employing the 'pseudo-inverse' concept developed by Deming and Devaney (1996). Using this approach, the matrix inversion becomes independent of the acquired data and, as a consequence, can be pre-computed and stored. Furthermore, the pseudo-inverse explicitly accounts for the band-limited nature of the acquired data and, for this reason, promises better images when a limited bandwidth and a small number of frequencies are used.

In the derivation of the imaging algorithm, it is assumed that the host formation is completely characterized by its conductivity and is manifested in the background wavenumber $k_0 \approx \sqrt{i\omega\mu_0\sigma_0}$. This assumption was made as a matter of convenience rather than necessity. Since this background wavenumber is complex, no complications arise from defining $k_0 = \sqrt{i\omega\mu_0(-i\omega\epsilon_0 + \sigma_0)}$ and thereby characterizing the host formation in terms of both its dielectric and conductivity. Similarly, the object function was assumed real, where $O(\boldsymbol{r}) = [(\sigma(\boldsymbol{r})/\sigma_0) - 1]$. The object function is, in general, complex, so that spatial variations in conductivity can be reconstructed from the real part of O, while spatial variations in dielectric can be reconstructed from $\mathrm{Im}(O)$.

Appendix. Introduction of ground–air planar interface effects

In section 2 the formulation for imaging a finite support heterogeneity from a suite of multimonostatic experiments with loop antennas scanning the $z = h, h \geqslant 0$ was presented, and it was assumed that the background conductivity (and dielectric) was the same for both half-spaces $z \geqslant 0$ and $z < 0$. The fact that the medium is a good conductor affects the formulation only in modifying the plane wavenumber from purely real in dielectric media to complex with a 45° phase. The 'propagation' effects are now called electromagnetic induction or diffusion, but other than terminology, nothing has essentially

changed compared to the electromagnetic dielectric case. A significant effect on the problem is that the generalized projection slice theorem (GPST) now relates plane wave spectra of scattered fields to the Fourier transform of the scatterer profile evaluated at complex spatial frequencies, a fact that poses special difficulties for the inverse (imaging) problem.

In this appendix, the work of section 2 is extended to the case where the scatterer is embedded in a conducting half space at $z < 0$, where the access for interrogating the object is limited to the adjacent free space at $z \geqslant 0$. It is assumed that the scatterer is sufficiently weak, such that its coupling to the $z = 0$ interface is negligible, and also that the antennas themselves are negligibly coupled to this interface (which is always true in the case of loop antennas that are sufficiently small compared to the wavelength and compared to their distance from the interface).

A.1. Dyadic Fresnel coefficients for transmission of plane electromagnetic waves through an air–ground interface

The geometry considered is shown in figure A.1 where the ground at $z < 0$ is characterized by a wavenumber $k_0 = (i\omega\mu_0\sigma_0)^{1/2}$ and the air at $z \geqslant 0$ is characterized by a purely real wavenumber $k_1 = \omega(\mu_0\epsilon_0)^{1/2}$.

The *scalar* Fresnel transmission coefficients are readily obtained through application of the continuity condition of the tangential electric field and its normal derivative across the boundary at $z = 0$

$$\begin{aligned} \tilde{T}_+(\boldsymbol{K}) &= \frac{2m_0}{m_0 + m_1} \qquad m_0(\boldsymbol{K}) = \sqrt{k_0^2 - K^2} \qquad \mathrm{Im}\{m_0\} \geqslant 0,\ \mathrm{Re}\{m_0\} \geqslant 0 \\ \tilde{T}_-(\boldsymbol{K}) &= \frac{2m_1}{m_0 + m_1} \qquad m_1(\boldsymbol{K}) = \sqrt{k_1^2 - K^2} \qquad \mathrm{Im}\{m_1\} \geqslant 0,\ \mathrm{Re}\{m_1\} \geqslant 0 \end{aligned} \tag{A.1}$$

such that the tangential electric fields are related through

$$\begin{aligned} (\mathcal{I} - \hat{z}\hat{z}) \cdot \tilde{\boldsymbol{E}}_1(\boldsymbol{K}) &= \tilde{T}_+(\boldsymbol{K})(\mathcal{I} - \hat{z}\hat{z}) \cdot \tilde{\boldsymbol{E}}_0^{\mathrm{inc}}(\boldsymbol{K}) \\ (\mathcal{I} - \hat{z}\hat{z}) \cdot \tilde{\boldsymbol{E}}_0(\boldsymbol{K}) &= \tilde{T}_-(\boldsymbol{K})(\mathcal{I} - \hat{z}\hat{z}) \cdot \tilde{\boldsymbol{E}}_1^{\mathrm{inc}}(\boldsymbol{K}). \end{aligned} \tag{A.2}$$

The *full* vector electric fields across the $z = 0$ boundary are thus related through a *dyadic* Fresnel transmission coefficient

$$\begin{aligned} \tilde{\boldsymbol{E}}_1(\boldsymbol{K}) &= \tilde{T}_+(\boldsymbol{K}) \cdot \tilde{\boldsymbol{E}}_0^{\mathrm{inc}}(\boldsymbol{K}) \qquad \tilde{T}_+(\boldsymbol{K}) = \left[\mathcal{I} - \hat{z}\left(\hat{z} + \frac{\boldsymbol{K}}{m_1(\boldsymbol{K})}\right)\right]\tilde{T}_+(\boldsymbol{K}) \\ \tilde{\boldsymbol{E}}_0(\boldsymbol{K}) &= \tilde{T}_-(\boldsymbol{K}) \cdot \tilde{\boldsymbol{E}}_1^{\mathrm{inc}}(\boldsymbol{K}) \qquad \tilde{T}_-(\boldsymbol{K}) = \left[\mathcal{I} - \hat{z}\left(\hat{z} - \frac{\boldsymbol{K}}{m_0(\boldsymbol{K})}\right)\right]\tilde{T}_-(\boldsymbol{K}) \end{aligned} \tag{A.3}$$

where the z components have been derived by invoking the transversality condition of the electric field with respect to the plane wavevector $(\boldsymbol{K} + m_1\hat{z}) \cdot \tilde{\boldsymbol{E}}_1(\boldsymbol{K}) = 0$ and $(\boldsymbol{K} - m_0\hat{z}) \cdot \tilde{\boldsymbol{E}}_0(\boldsymbol{K}) = 0$.

A.2. Scattered electric field within the Born approximation in the presence of a planar boundary

In section 2, it was shown (8) that the plane wave spectrum of the scattered field at $z = 0$, due to a source antenna positioned at $\boldsymbol{r}_0$ in a homogeneous background k_0, is given by

$$\begin{aligned} \tilde{\boldsymbol{E}}^{\mathrm{s}}(\boldsymbol{K}'; \boldsymbol{r}_0) &= (\mathcal{I} - \hat{\boldsymbol{k}}'_{0+}\hat{\boldsymbol{k}}'_{0+}) \cdot \frac{\mathrm{i}}{2m'_0} \int \mathrm{d}\boldsymbol{K}\, \tilde{\boldsymbol{E}}_0(\boldsymbol{K}; \boldsymbol{r}_0) \int \mathrm{d}\boldsymbol{r}'\, f(\boldsymbol{r}')\, \mathrm{e}^{-\mathrm{i}(\boldsymbol{k}'_{0+} - \boldsymbol{k}_{0-}) \cdot \boldsymbol{r}'} \\ \tilde{\boldsymbol{E}}_0(\boldsymbol{K}; \boldsymbol{r}_0) &= \tilde{\boldsymbol{E}}_0(\boldsymbol{K})\, \mathrm{e}^{-\mathrm{i}\boldsymbol{k}_{0-} \cdot \boldsymbol{r}_0} \end{aligned} \tag{A.4}$$

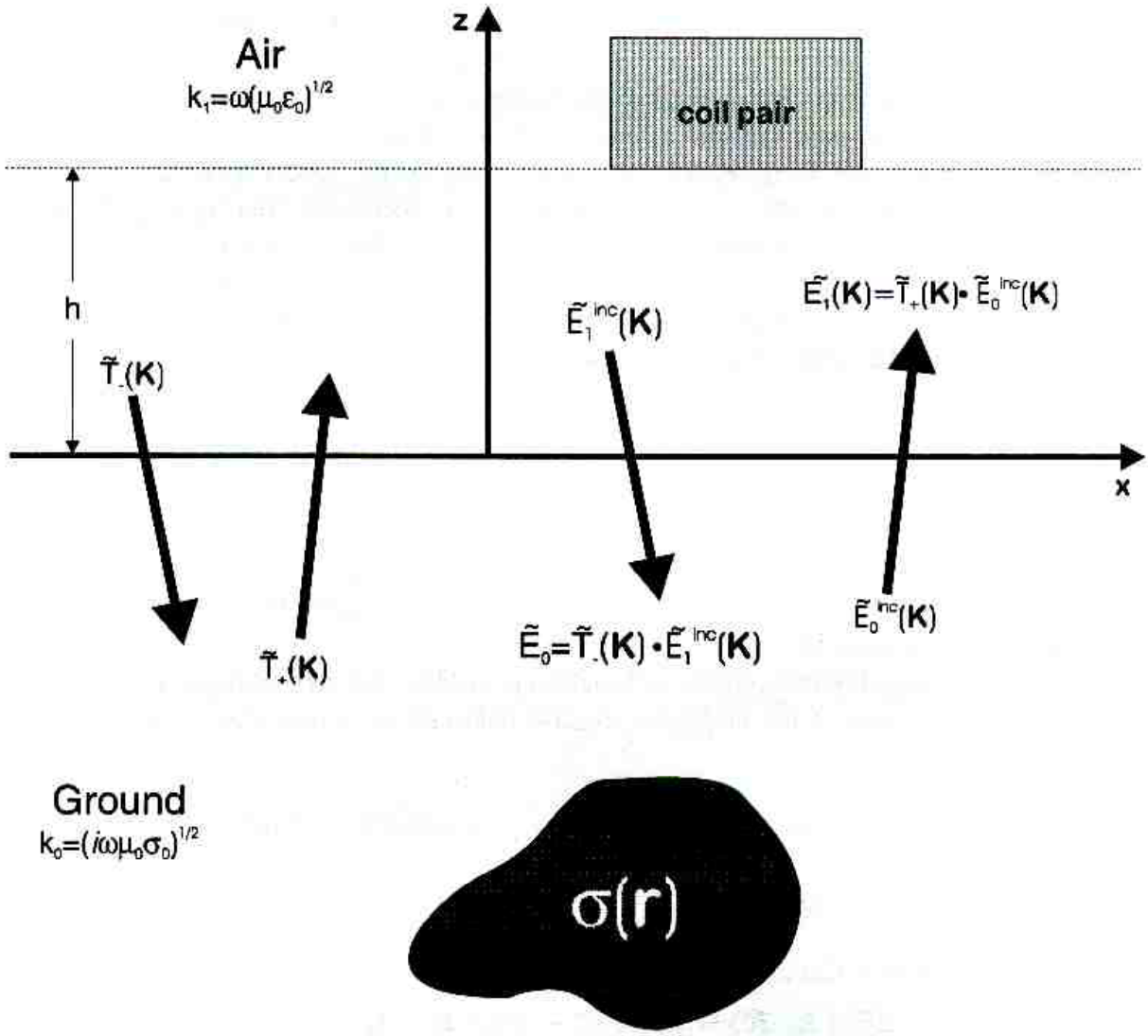

Figure A.1. Plane wave spectral relations at an interface between air and ground for the geometry under consideration.

where

$$\boldsymbol{k}_{0\pm}(\boldsymbol{K}) = \boldsymbol{K} \pm m_0(\boldsymbol{K})\hat{\boldsymbol{z}} \qquad m_0(\boldsymbol{K}) = \sqrt{k_0^2 - K^2} \qquad \mathrm{Im}\{m_0\} \geqslant 0 \qquad K = |\boldsymbol{K}|$$
$$\boldsymbol{k}'_{0\pm} = \boldsymbol{k}_{0\pm}(\boldsymbol{K}') \qquad m'_0 = m_0(\boldsymbol{K}') \tag{A.5}$$

and $\tilde{\boldsymbol{E}}_0(\boldsymbol{K})$ is the plane wave spectrum of the electric field emitted by the source antenna when positioned at reference location $\boldsymbol{r}_0 = 0$. $\tilde{\boldsymbol{E}}^s(\boldsymbol{K}'; \boldsymbol{r}_0)$ is the plane wave spectrum of the scattered field at $z = 0$ when the source antenna is located at $\boldsymbol{r}_0$.

If it is assumed that the upper half space $z \geqslant 0$ is free space $k_1 \neq k_0$, and also assumed that the scatterer is negligibly coupled to the $z = 0$ interface, then the above equation provides an expression for the scattered field incident on the $z = 0^-$ boundary with $\tilde{\boldsymbol{E}}_0$ being the source field transmitted into the lower domain at $z = 0^-$. In terms of the electric fields at $z = 0^+$,

$$\tilde{\boldsymbol{E}}_1^s(\boldsymbol{K}'; \boldsymbol{r}_0) = \tilde{\boldsymbol{T}}_+(\boldsymbol{K}')(\mathcal{I} - \hat{\boldsymbol{k}}'_{0+}\hat{\boldsymbol{k}}'_{0+}) \cdot \frac{\mathrm{i}}{2m'_0} \int \mathrm{d}\boldsymbol{K}\, \tilde{\boldsymbol{T}}_-(\boldsymbol{K})\tilde{\boldsymbol{E}}_1^{\mathrm{inc}}(\boldsymbol{K}; \boldsymbol{r}_0)$$
$$\times \int \mathrm{d}\boldsymbol{r}'\, f(\boldsymbol{r}')\, \mathrm{e}^{-\mathrm{i}(\boldsymbol{k}'_{0+} - \boldsymbol{k}_{0-})\cdot\boldsymbol{r}'}$$

$$\tilde{\boldsymbol{E}}_1^{\text{inc}}(\boldsymbol{K}; \boldsymbol{r}_0) = \tilde{\boldsymbol{E}}^{\text{inc}}(\boldsymbol{K})\, \mathrm{e}^{-\mathrm{i}\boldsymbol{k}_{1-}\cdot\boldsymbol{r}_0} \tag{A.6}$$

where the plane wavevector in the upper half space is defined by

$$\boldsymbol{k}_{1\pm} = \boldsymbol{K} \pm m_1(\boldsymbol{K})\hat{\boldsymbol{z}} \qquad m_1(\boldsymbol{K}) = (k_1^2 - K^2)^{1/2} \qquad \mathrm{Im}\{m_1\} \geqslant 0. \tag{A.7}$$

For later use, it is desirable to Fourier transform $\boldsymbol{x}_0$, the lateral spatial variable of $\boldsymbol{r}_0$, according to

$$\tilde{\tilde{\boldsymbol{E}}}_1^{\text{s}}(\boldsymbol{K}'; \boldsymbol{K}, z_0) = \int \mathrm{d}\boldsymbol{x}_0\, \mathrm{e}^{-\mathrm{i}\boldsymbol{K}\cdot\boldsymbol{x}_0} \tilde{\boldsymbol{E}}_1^{\text{s}}(\boldsymbol{K}'; \boldsymbol{x}_0, z_0) \tag{A.8}$$

to obtain the doubly Fourier-transformed multimonostatic scattered field

$$\begin{aligned} \tilde{\tilde{\boldsymbol{E}}}_1^{\text{s}}(\boldsymbol{K}'; \boldsymbol{K}, z_0) &= (2\pi)^{c-1} \frac{\mathrm{i}}{2m_0'} \mathrm{e}^{\mathrm{i}m_1 z_0} \tilde{\mathcal{D}}(\boldsymbol{K}'; \boldsymbol{K}) \cdot \tilde{\boldsymbol{E}}_1^{\text{inc}}(-\boldsymbol{K})\, \tilde{\tilde{f}}(\boldsymbol{k}_{0+}' + \boldsymbol{k}_{0+}) \\ \tilde{\mathcal{D}}(\boldsymbol{K}'; \boldsymbol{K}) &= \tilde{\mathcal{T}}_+(\boldsymbol{K}')(\mathcal{I} - \hat{\boldsymbol{k}}_{0+}'\hat{\boldsymbol{k}}_{0+}')\tilde{\mathcal{T}}_-(-\boldsymbol{K}) \end{aligned} \tag{A.9}$$

where the c-dimensional Fourier transform of the object function is defined according to

$$\tilde{\tilde{f}}(\boldsymbol{q}) = \int \mathrm{d}\boldsymbol{r}\, \mathrm{e}^{-\mathrm{i}\boldsymbol{q}\cdot\boldsymbol{r}} f(\boldsymbol{r}). \tag{A.10}$$

The doubly transformed multimonostatic scattered field referenced to $z_0 = 0$ is therefore given by

$$\tilde{\tilde{\boldsymbol{E}}}_1^{\text{s}}(\boldsymbol{K}'; \boldsymbol{K}) = (2\pi)^{c-1} \frac{\mathrm{i}}{2m_0'} \tilde{\mathcal{D}}(\boldsymbol{K}'; \boldsymbol{K}) \cdot \tilde{\boldsymbol{E}}_1^{\text{inc}}(-\boldsymbol{K})\, \tilde{\tilde{f}}(\boldsymbol{k}_{0+}' + \boldsymbol{k}_{0+}). \tag{A.11}$$

As found in section 2, the plane wave spectrum of the transmitting antenna (subscripted by 0) field is related to its vector effective height $\tilde{\boldsymbol{h}}_0$ through

$$\tilde{\boldsymbol{E}}_1^{\text{inc}}(\boldsymbol{K}) = -I_0 \frac{\omega\mu_0}{2m_1} \tilde{\boldsymbol{h}}_0(-\boldsymbol{K}) \tag{A.12}$$

such that, in terms of the vector effective height of the transmitting antenna, it is given by the following expression for the doubly Fourier-transformed multimonostatic scattered electric field

$$\tilde{\tilde{\boldsymbol{E}}}_1^{\text{s}}(\boldsymbol{K}'; \boldsymbol{K}) = -(2\pi)^{c-1} I_0 \frac{\mathrm{i}\omega\mu_0}{4m_1 m_0'} \tilde{\mathcal{D}}(\boldsymbol{K}'; \boldsymbol{K}) \cdot \tilde{\boldsymbol{h}}_0(\boldsymbol{K})\, \tilde{\tilde{f}}(\boldsymbol{k}_{0+}' + \boldsymbol{k}_{0+}). \tag{A.13}$$

Note that this is only the component of the field scattered off the interior of $z < 0$ and does not contain the undesired (strong) component of the field reflected off the $z = 0$ boundary as well as the direct field. The undesired components can be easily incorporated into the formulation or, alternatively, if illuminating the ground with short pulses, the early arrival of these components can be effectively time gated.

A.3. Measured signal in a multimonostatic measurement configuration above ground

In this section we obtain the terminal signal at a receiving antenna, that sweeps a plane $z = z_0$ in synchronization with the transmitting antenna that is excited with a terminal current I_0.

Assuming that the scattered signal $\tilde{\boldsymbol{E}}_1^s(\boldsymbol{K}; \boldsymbol{r}_0)$ is received by a receiving antenna that is positioned at $\boldsymbol{r}_1$ such that if it were to transmit, its current distribution would be $\boldsymbol{J}_1(\boldsymbol{r}-\boldsymbol{r}_1)$, with terminal current I_1. By the Lorentz reciprocity theorem, it is known that the open circuit terminal voltage is given by

$$\begin{aligned} V(\boldsymbol{r}_1; \boldsymbol{r}_0) &= -\frac{1}{I_1}\int \mathrm{d}\boldsymbol{r}'\, \boldsymbol{J}_1(\boldsymbol{r}'-\boldsymbol{r}_1)\cdot \boldsymbol{E}_1^s(\boldsymbol{r}'; \boldsymbol{r}_0) = -\frac{1}{I_1}\int \mathrm{d}\boldsymbol{r}'\, \boldsymbol{J}_1(\boldsymbol{r}')\cdot \boldsymbol{E}_1^s(\boldsymbol{r}'+\boldsymbol{r}_1; \boldsymbol{r}_0) \\ &= -(2\pi)^{1-c}\frac{1}{I_1}\int \mathrm{d}\boldsymbol{r}'\, \boldsymbol{J}_1(\boldsymbol{r}')\cdot \int \mathrm{d}\boldsymbol{K}'\, \mathrm{e}^{\mathrm{i}\boldsymbol{K}'\cdot(\boldsymbol{x}'+\boldsymbol{x}_1)}\tilde{\boldsymbol{E}}_1^s(\boldsymbol{K}'; \boldsymbol{r}_0)\, \mathrm{e}^{\mathrm{i}m_1'(z'+z_1)} \\ &= -(2\pi)^{1-c}\int \mathrm{d}\boldsymbol{K}'\, \tilde{\boldsymbol{h}}_1(\boldsymbol{K}')\cdot \tilde{\boldsymbol{E}}_1^s(\boldsymbol{K}'; \boldsymbol{r}_0)\, \mathrm{e}^{\mathrm{i}\boldsymbol{k}_{1+}'\cdot\boldsymbol{r}_1} \\ &= -(2\pi)^{2(1-c)}\int \mathrm{d}\boldsymbol{K}'\, \tilde{\boldsymbol{h}}_1(\boldsymbol{K}')\cdot \int \mathrm{d}\boldsymbol{K}\; \tilde{\tilde{\boldsymbol{E}}}_1^s(\boldsymbol{K}'; \boldsymbol{K})\, \mathrm{e}^{\mathrm{i}(\boldsymbol{k}_{1+}'\cdot\boldsymbol{r}_1+\boldsymbol{k}_{1+}\cdot\boldsymbol{r}_0)} \end{aligned} \tag{A.14}$$

where the vector effective height of the antenna for fields arriving from $z<0$ is defined in the usual way (13)

$$\tilde{\boldsymbol{h}}_1(\boldsymbol{K}') = (\mathcal{I}-\hat{\boldsymbol{k}}_{1+}'\hat{\boldsymbol{k}}_{1+}')\cdot\frac{1}{I_1}\int \mathrm{d}\boldsymbol{r}'\, \boldsymbol{J}_1(\boldsymbol{r}')\, \mathrm{e}^{\mathrm{i}\boldsymbol{k}_{1+}'\cdot\boldsymbol{r}'}. \tag{A.15}$$

To this point, the measured signal is at $\boldsymbol{r}_1$ due to a source located at $\boldsymbol{r}_0$. In the multimonostatic case, $\boldsymbol{r}_1=\boldsymbol{r}_0$, such that

$$V(\boldsymbol{r}_0; \boldsymbol{r}_0) = V_{\mathrm{mm}}(\boldsymbol{r}_0) = -(2\pi)^{2(1-c)}\int \mathrm{d}\boldsymbol{K}'\, \tilde{\boldsymbol{h}}_1(\boldsymbol{K}')\cdot \int \mathrm{d}\boldsymbol{K}\; \tilde{\tilde{\boldsymbol{E}}}_1^s(\boldsymbol{K}'; \boldsymbol{K})\, \mathrm{e}^{\mathrm{i}(\boldsymbol{k}_{1+}'+\boldsymbol{k}_{1+})\cdot\boldsymbol{r}_0} \tag{A.16}$$

where V_{mm} denotes the multimonostatic signal (now dependent on only one set of coordinates). Finally, Fourier transforming with respect to the $\boldsymbol{x}_0$ variable gives

$$\tilde{V}_{\mathrm{mm}}(\boldsymbol{K}, z_0) = -(2\pi)^{1-c}\int \mathrm{d}\boldsymbol{K}'\, \mathrm{e}^{\mathrm{i}[m_1'+m_1(\boldsymbol{K}-\boldsymbol{K}')]z_0}\tilde{\boldsymbol{h}}_1(\boldsymbol{K}')\cdot\tilde{\tilde{\boldsymbol{E}}}_1^s(\boldsymbol{K}'; \boldsymbol{K}-\boldsymbol{K}'). \tag{A.17}$$

Now, substituting the expression for the doubly Fourier-transformed field (A.13) yields

$$\begin{aligned} \tilde{V}_{\mathrm{mm}}(\boldsymbol{K}, z_0)/I_0 = \frac{\mathrm{i}\omega\mu_0}{4}\int \mathrm{d}\boldsymbol{K}'\, &\frac{\mathrm{e}^{\mathrm{i}[m_1'+m_1(\boldsymbol{K}-\boldsymbol{K}')]z_0}}{m_1(\boldsymbol{K}-\boldsymbol{K}')m_0'}\tilde{\boldsymbol{h}}_1(\boldsymbol{K}')\cdot\tilde{\mathcal{D}}(\boldsymbol{K}'; \boldsymbol{K}-\boldsymbol{K}') \\ &\cdot\tilde{\boldsymbol{h}}_0(\boldsymbol{K}-\boldsymbol{K}')\; \tilde{\tilde{f}}[\boldsymbol{k}_{0+}'+\boldsymbol{k}_{0+}(\boldsymbol{K}-\boldsymbol{K}')]. \end{aligned} \tag{A.18}$$

This result is in agreement with (15) when z_0 is set to zero and the Fresnel transmission dyads are set to unity. Compared to the result in section 2 (equation (15)), here the effect of the $z=0$ interface is embodied in the dyadic denoted by $\tilde{\mathcal{D}}$.

This result relates $\tilde{V}(\boldsymbol{K})$ to the Fourier transform of the object function at spatial frequencies $\boldsymbol{k}_{0+}(\boldsymbol{K}')+\boldsymbol{k}_{0+}(\boldsymbol{K}-\boldsymbol{K}')$. It is the $\boldsymbol{K}'$ integral that prevents this last equation from being an ordinary projection slice theorem relation.

References

Deming R and Devaney A J 1996 A filtered backpropagation algorithm for GPR *J. Env. Eng. Geophys.* **0** 113–24

Devaney A J 1982 A filtered backpropagation algorithm for diffraction tomography *Ultrasonic Imaging* **4** 336–50

——1984 Geophysical diffraction tomography *IEEE Trans. Geosci. Remote Sensing* **GE-22** 3–13

Molyneux J E and Witten A J 1993 Diffraction tomographic imaging in a monostatic measurement geometry *IEEE Trans. Geosci. Remote Sensing* **31** 507–10

Morse P M and Feshbach H 1953 *Methods of Theoretical Physics* (New York: McGraw-Hill)

Norton S J and Bowler J R 1993 The theory of eddy current inversion *J. Appl. Phys.* **73** 501–12

Press W H, Teukolsky S A, Vetterling W T and Flannery B P 1992 *Numerical Recipes* 2nd edn (Cambridge: Cambridge University Press)

Witten A J, Molyneux J E and Nyquist J 1994 Ground penetrating radar tomography: algorithms and case studies *IEEE Trans. Geosci. Remote Sensing* **32** 461–7

Witten A J, Schatzberg A and Devaney A J 1994 Signal processing of electromagnetic induction data for tunnel detection *National Security Programs Office Report* K/NSP-208

Won I J 1980 A wide-band electromagnetic exploration method: some theoretical and experimental results *Geophys.* **45** 928–40

Won I J, Keiswetter D A, Fields G R A and Sutton L C 1996 GEM-2: a new multifrequency electromagnetic sensor *J. Env. Eng. Geophys.* **1** 129–37